



# Novel 3DOM-SrTiO<sub>3</sub>/Ag/Ag<sub>3</sub>PO<sub>4</sub> ternary Z-scheme photocatalysts with remarkably improved activity and durability for contaminant degradation



Chenxi Zhang<sup>a,b</sup>, Kai Yu<sup>b,\*</sup>, Yajun Feng<sup>b</sup>, Yue Chang<sup>a,b</sup>, Ting Yang<sup>a</sup>, Ying Xuan<sup>b</sup>, Da Lei<sup>a,b</sup>, Lan-Lan Lou<sup>a</sup>, Shuangxi Liu<sup>a,c,\*\*</sup>

<sup>a</sup> Institute of New Catalytic Materials Science and MOE Key Laboratory of Advanced Energy Materials Chemistry, School of Materials Science and Engineering, National Institute of Advanced Materials, Nankai University, Tianjin 300350, People's Republic of China

<sup>b</sup> MOE Key Laboratory of Pollution Processes and Environmental Criteria, College of Environmental Science and Engineering, Nankai University, Tianjin 300350, People's Republic of China

<sup>c</sup> Collaborative Innovation Center of Chemical Science and Engineering (Tianjin), Tianjin 300072, People's Republic of China

## ARTICLE INFO

### Article history:

Received 17 January 2017

Received in revised form 7 March 2017

Accepted 22 March 2017

Available online 24 March 2017

### Keywords:

3DOM-SrTiO<sub>3</sub>/Ag/Ag<sub>3</sub>PO<sub>4</sub> ternary composites

Inverse opal

Z-scheme photocatalyst

Slow photon effect

Photodegradation

## ABSTRACT

The novel visible-light-driven 3DOM-SrTiO<sub>3</sub>/Ag/Ag<sub>3</sub>PO<sub>4</sub> ternary composites were fabricated and used as photocatalysts in the degradation of organic contaminants, including RhB, phenol, and MB. Through the XRD, SEM, TEM, DR UV-vis, XPS, PL spectroscopy, N<sub>2</sub> sorption, and photoelectrochemical measurement, the obtained 3DOM-SrTiO<sub>3</sub>/Ag/Ag<sub>3</sub>PO<sub>4</sub> ternary composites were well characterized. The effects of SrTiO<sub>3</sub>:Ag<sub>3</sub>PO<sub>4</sub> molar ratio and stop-bands of 3DOM-SrTiO<sub>3</sub> on the catalytic performance were systematically investigated. 3DOM-SrTiO<sub>3</sub>/Ag/Ag<sub>3</sub>PO<sub>4</sub> ternary composite photocatalysts exhibited notably enhanced activity compared with single 3DOM-SrTiO<sub>3</sub> and Ag<sub>3</sub>PO<sub>4</sub> catalyst. Among these ternary photocatalysts, S35A65(300) exhibited the most excellent photocatalytic performance under visible light irradiation, which could be mainly attributed to synergy effect of the notably improved separate efficiency of photogenerated electron-hole pairs and the suitable stop-bands of 3DOM-SrTiO<sub>3</sub>(300) material. Although the gradually reduced activity in cycling tests was obtained over S35A65(300) under visible light irradiation, an excellent durability could be achieved for S35A65(300) under UV-vis light irradiation. No obvious loss in photocatalytic efficiency was observed after six cycles for RhB degradation. The notably improved enhanced durability of 3DOM-SrTiO<sub>3</sub>/Ag/Ag<sub>3</sub>PO<sub>4</sub> ternary composites under UV-vis light irradiation could be mainly attributed to the Z-scheme mechanism of this ternary composite photocatalyst.

© 2017 Elsevier B.V. All rights reserved.

## 1. Introduction

Photocatalysis has been recognized as one of the most promising approaches toward solving both energy and environmental pollution problems in the future [1–6]. Among the reported photocatalysts, strontium titanate (SrTiO<sub>3</sub>) as a typical perovskite structured material has been widely studied because of its structural flexibility, good stability, low toxicity and efficient photocatalytic activity [7–13]. However, the wide band gap of SrTiO<sub>3</sub> (about 3.2 eV) limited its application in visible-light-driven photocatalytic degradation of contaminants or water splitting. Therefore, many researches had been reported focused on the improvement of

its visible light harvesting ability, including energy-band engineering [14–16], morphology control [17–21], compositing with narrow band-gap semiconductor [22–24], surface treatment [25,26], and so on.

In the last decade, the three-dimensionally ordered macroporous (3DOM) materials have received much attention in photocatalysis field because of their characteristic slow photon effect, which could delay and store the incident light with certain wavelengths in 3DOM materials, and significantly improve their light harvesting efficiency [27–30]. Many 3DOM photocatalysts, such as TiO<sub>2</sub> [31–45], InVO<sub>4</sub> [46–48], WO<sub>3</sub> [49–51], BiVO<sub>4</sub> [52,53], Bi<sub>2</sub>WO<sub>6</sub> [54], SnO<sub>2</sub> [55,56], ZnGa<sub>2</sub>O<sub>4</sub> [57] and g-C<sub>3</sub>N<sub>4</sub> [44] have been prepared and employed as photocatalysts for the degradation of contaminants and water splitting. Recently, we reported the 3DOM-SrTiO<sub>3</sub> photocatalyst [58], which exhibited notably enhanced photocatalytic performance for water splitting hydro-

\* Corresponding author.

\*\* Corresponding author.

E-mail addresses: [kaiyu@nankai.edu.cn](mailto:kaiyu@nankai.edu.cn) (K. Yu), [sliu@nankai.edu.cn](mailto:sliu@nankai.edu.cn) (S. Liu).

gen evolution compared with ever reported mesoporous SrTiO<sub>3</sub> and solid-state SrTiO<sub>3</sub> photocatalysts. However, the wide band gap of these 3DOM-SrTiO<sub>3</sub> materials led to their poor photocatalytic performance under visible light irradiation.

Silver phosphate (Ag<sub>3</sub>PO<sub>4</sub>), as a highly efficient visible-light-driven photocatalyst, has been drawn tremendous attention when it was reported by Ye et al. [59–65]. It could not only oxidize water to produce oxygen but also degrade organic contaminants under visible light irradiation. While, the stability issue of Ag<sub>3</sub>PO<sub>4</sub> always puzzled the researchers [66]. Many strategies have been made to improve the stability of Ag<sub>3</sub>PO<sub>4</sub> [66]. Among these reports, fabrication of heterojunction catalysts with other semiconductors was an efficient method to enhance the activity and stability of Ag<sub>3</sub>PO<sub>4</sub> [67–76] through the transfer and separation of photogenerated electrons and holes. For example, Guo et al. [76] reported an Ag<sub>3</sub>PO<sub>4</sub>/Cr-SrTiO<sub>3</sub> heterojunction photocatalyst with improved activity in isopropyl alcohol degradation compared with Ag<sub>3</sub>PO<sub>4</sub> and Cr-SrTiO<sub>3</sub>. Guan et al. [77] synthesized a series of SrTiO<sub>3</sub>/Ag<sub>3</sub>PO<sub>4</sub> composites with improved photocatalytic performance compared with Ag<sub>3</sub>PO<sub>4</sub>. The enhanced photocatalytic activity of these SrTiO<sub>3</sub>/Ag<sub>3</sub>PO<sub>4</sub> composites could be ascribed to the accelerated charge separation efficiency.

In this work, the visible-light-driven 3DOM-SrTiO<sub>3</sub>/Ag/Ag<sub>3</sub>PO<sub>4</sub> ternary composites were firstly synthesized and used as photocatalysts in the degradation of organic contaminants, including RhB, MB and phenol. The influences of 3DOM-SrTiO<sub>3</sub> stop-bands and SrTiO<sub>3</sub>:Ag<sub>3</sub>PO<sub>4</sub> molar ratio on the catalytic performance of these composite photocatalysts were systematically investigated. A highly improved visible-light photocatalytic performance was expected over these 3DOM-SrTiO<sub>3</sub>/Ag/Ag<sub>3</sub>PO<sub>4</sub> ternary composites because of the synergic effect of accelerated charge separation and enhanced light harvesting. In addition, when UV-vis light was used as light source, a Z-scheme charge transfer in these 3DOM-SrTiO<sub>3</sub>/Ag/Ag<sub>3</sub>PO<sub>4</sub> ternary composites could significantly improve the stability of these composite photocatalysts.

## 2. Experimental

### 2.1. Materials

Methyl methacrylate (MMA, stabilized with 30 ppm MEHQ), tetrabutyl titanate [Ti(OBu)<sub>4</sub>] and silver nitrate (AgNO<sub>3</sub>) were obtained from Aladdin. Strontium nitrate [Sr(NO<sub>3</sub>)<sub>2</sub>] was purchased from Tianjin Bodi Chemical Co., Ltd. Potassium persulfate (K<sub>2</sub>S<sub>2</sub>O<sub>8</sub>), disodium hydrogen phosphate (Na<sub>2</sub>HPO<sub>4</sub>) and citric acid monohydrate (C<sub>6</sub>H<sub>8</sub>O<sub>7</sub>·H<sub>2</sub>O) were supplied by Sinopharm Chemical Reagent Co., Ltd. Acetic acid, dimethyl sulfoxide (DMSO), and isopropanol (IPA) were acquired from Concord Technology (Tianjin) Co., Ltd. Rhodamine B (RhB), methylene blue (MB) and phenol were obtained from Tianjin Heowns Biochemical Technology Co., Ltd. Nafion® 117 solution (~5% in a mixture of lower aliphatic alcohols and water) was purchased from Sigma-Aldrich. 1,4-Benzenequinone (BQ) was supplied by Energy Chemical. Ethylenediaminetetraacetic acid disodium salt (EDTA-2Na) was acquired from Tianjin Guangfu Technology Development Co., Ltd. 5,5-Dimethyl-1-pyrroline N-oxide (DMPO) was purchased from Meryer (Shanghai) Chemical Technology Co., Ltd.

### 2.2. Characterization

The morphology of these obtained samples were observed from a JEOL JSM-7500F field-emission scanning electron microscope (SEM) and a Philips Tecnai G2 F30 high-resolution transmission electron microscope (HRTEM). A Bruker D8 X-ray diffractometer with Cu K $\alpha$  radiation was used to record the X-ray powder

diffraction (XRD) patterns at a scan rate of 0.01°/s, the operation voltage and current remained 40 kV and 40 mA, respectively. N<sub>2</sub> sorption analysis of these photocatalysts was performed on a Micromeritics TriStar 3000 sorptometer and the surface areas were determined by BET method. Diffuse-reflectance UV-vis (DR UV-vis) spectra were obtained on a Shimadzu UV-2550 spectrophotometer with an integral sphere employing BaSO<sub>4</sub> as a reference in the measurement range from 200 nm to 800 nm. X-ray photoelectron spectroscopy (XPS) spectra were recorded on a Kratos Axis Ultra DLD with an Al K $\alpha$  X-ray source. Photoluminescence (PL) spectra of the as-prepared samples were measured using an Edinburgh Instruments FLS 920P fluorescence spectrophotometer. The electron spin resonance (ESR) characterization of these photocatalysts was performed on a MagnetTech Miniscope MS400 spectrometer by Freiberg Instruments.

### 2.3. Synthesis of 3DOM-SrTiO<sub>3</sub>/Ag/Ag<sub>3</sub>PO<sub>4</sub> composite photocatalysts

#### 2.3.1. Synthesis of 3DOM-SrTiO<sub>3</sub> and disordered porous SrTiO<sub>3</sub> materials

3DOM-SrTiO<sub>3</sub> samples were synthesized through a polymethylmethacrylate (PMMA) colloidal crystal template method according to our previous works [51,58]. The PMMA colloidal crystal templates were assembled by a centrifugation method using PMMA microspheres with average diameters of 200 nm, 300 nm, and 400 nm. The SEM images of these PMMA colloidal crystal templates are described in Fig. S1 of Supplementary materials.

The precursor solution of SrTiO<sub>3</sub> was prepared as follows. 10 mL of deionized water was dropped into the mixture of tetrabutyl titanate (0.01 mol) and acetic acid (10 mL) under stirring. Then the aqueous solution of Sr(NO<sub>3</sub>)<sub>2</sub> (0.01 mol in 10 mL of H<sub>2</sub>O) and citric acid (0.02 mol in 10 mL of H<sub>2</sub>O) were sequentially added dropwise into the reaction solution. After 30 min of stirring at room temperature, a clear precursor solution of SrTiO<sub>3</sub> was obtained.

In order to prepare 3DOM-SrTiO<sub>3</sub> with different pore size, the PMMA colloidal crystal templates with different diameters were soaked into the SrTiO<sub>3</sub> precursor solution for 2 h. After filtration, the sample powders were dried at 50 °C under vacuum and calcined in a muffle furnace at 650 °C for 4 h to remove the PMMA template. According to the diameter of PMMA colloidal crystal template, the obtained 3DOM-SrTiO<sub>3</sub> materials were denoted as 3DOM-SrTiO<sub>3</sub>(x) (x = 200, 300, or 400).

For comparison, a disordered porous SrTiO<sub>3</sub> material (denoted as D-SrTiO<sub>3</sub>) was synthesized using same conditions with that of 3DOM-SrTiO<sub>3</sub>, except that a disordered PMMA polymer microsphere template was used in this process.

#### 2.3.2. Synthesis of 3DOM-SrTiO<sub>3</sub>/Ag/Ag<sub>3</sub>PO<sub>4</sub> composites

3DOM-SrTiO<sub>3</sub>/Ag/Ag<sub>3</sub>PO<sub>4</sub> composites were synthesized through a deposition-precipitation method. A certain amount of AgNO<sub>3</sub> was dissolved into a mixture solution of deionized water (12.5 mL) and DMSO (25 mL). Then 3DOM-SrTiO<sub>3</sub>(x) was added into the solution. After stirring at room temperature for 15 min, a certain amount of Na<sub>2</sub>HPO<sub>4</sub> aqueous solution (0.15 M) was added dropwise into this reaction mixture. The resulted mixture was continuously stirred for 30 min and separated by centrifugation. The obtained composites were collected and washed with deionized water, and then dried at 55 °C under vacuum. The molar ratio of 3DOM-SrTiO<sub>3</sub> to Ag<sub>3</sub>PO<sub>4</sub> was controlled by the dosage of AgNO<sub>3</sub>, Na<sub>2</sub>HPO<sub>4</sub>, and 3DOM-SrTiO<sub>3</sub>. Table 1 lists the composition of these reaction solutions. The obtained composites were marked as SmAn(x) (x = 200, 300, or 400), in which m and n are the molar percentage of 3DOM-SrTiO<sub>3</sub> and Ag<sub>3</sub>PO<sub>4</sub> based on the feeding amount, respectively. However, because of the photo corrosion of Ag<sub>3</sub>PO<sub>4</sub>, a few of Ag nanoparticles could be generated

**Table 1**

The composition of reaction solution for the preparation of 3DOM-SrTiO<sub>3</sub>/Ag/Ag<sub>3</sub>PO<sub>4</sub> composites.

Sample	Amount of AgNO <sub>3</sub> (g)	Amount of 3DOM-SrTiO <sub>3</sub> (x) (g)	Volume of Na <sub>2</sub> HPO <sub>4</sub> solution (mL)
S30A70(x)	0.14	0.0216	7.0
S35A65(x)	0.13	0.0252	6.5
S40A60(x)	0.12	0.0288	6.0
S50A50(x)	0.10	0.0360	5.0
S60A40(x)	0.08	0.0432	4.0
S70A30(x)	0.06	0.0504	3.0

on the surface of Ag<sub>3</sub>PO<sub>4</sub> during the synthesis process of these composites. Actually, the as-synthesized composite photocatalysts were 3DOM-SrTiO<sub>3</sub>/Ag/Ag<sub>3</sub>PO<sub>4</sub> ternary composites. Similarly, the D-SrTiO<sub>3</sub>/Ag/Ag<sub>3</sub>PO<sub>4</sub> composites could be synthesized under the same conditions, and these catalysts were marked as DS<sub>m</sub>An according to the different molar percentage of D-SrTiO<sub>3</sub> and Ag<sub>3</sub>PO<sub>4</sub>.

#### 2.4. Photoelectrochemical measurement

The photoelectrochemical measurement was carried out on a conventional three-electrode cell by using computer-controlled electrochemical workstation (CHI 660D). Typically, 5.0 mg of catalyst was suspended in deionized water (160 μL), and then, 4.0 μL of Nafion® 117 solution was added to the above dispersion. After ultrasonic treatment for 2 min, the obtained homogeneous suspension (0.1 mL) was dropped onto the surface of Fluorine doped tin oxide (FTO) glass (1.0 × 1.0 cm). The FTO glass with samples was used as the working electrode. The Pt plate and Ag/AgCl electrode were used as the counter electrode and the reference electrode, respectively. 0.1 M sodium sulfate was used as the electrolyte in this three-electrode cell. The current-time (I-t) curves were collected at the open-circuit potential. The light source was a 300 W Xe lamp equipped with a UV cutoff filter ( $\lambda > 420$  nm).

#### 2.5. Photocatalytic degradation of organic contaminants

The photocatalytic activities of these photocatalysts were evaluated by the degradation of organic contaminants including RhB, MB and phenol under visible light irradiation. In a typical process, 50 mL of organic contaminant solution and 50 mg of photocatalyst were mixed and magnetically stirred in the 200 mL quartz photo reactor in the dark for 30 min to establish an adsorption–desorption equilibrium. Then, the suspended solution was irradiated by a 300 W Xe lamp with a cutoff filter of 420 nm. After the photodegradation experiment, the photocatalyst was separated from the reaction solution by centrifugation, thoroughly washed, and then reused in the following run. The concentrations of organic contaminant were determined by the UV-vis spectrophotometry and HPLC.

The concentrations of RhB and MB in water were detected by a Shimadzu UV-2550 UV-vis spectrophotometer at the wavelength of maximum absorption. The concentration of phenol in water was determined by an Agilent 1200 series high-performance liquid chromatograph (HPLC) equipped with an Agilent XDB-C18 column and a UV detector (270 nm for phenol). The mobile phase was a mixture of acetonitrile and water (50/50, v/v), and was pumped at a flow rate of 0.7 mL/min. The corresponding UV-vis spectra and HPLC profiles of these organic contaminants under photocatalytic process are described in Figs. S2 and S3 of Supplementary Materials.

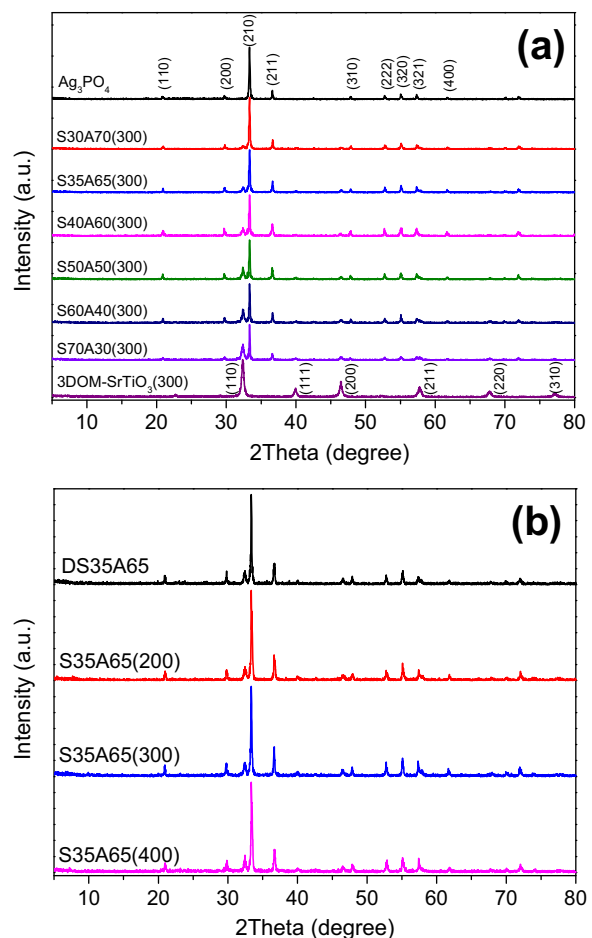


**Fig. 1.** Powder XRD patterns of these as-synthesized 3DOM-SrTiO<sub>3</sub>/Ag/Ag<sub>3</sub>PO<sub>4</sub> composites.

## 3. Results and discussion

### 3.1. Characterization of 3DOM-SrTiO<sub>3</sub>/Ag/Ag<sub>3</sub>PO<sub>4</sub> composites

The as-synthesized 3DOM-SrTiO<sub>3</sub>/Ag/Ag<sub>3</sub>PO<sub>4</sub> composite photocatalysts were characterized by XRD, SEM, TEM, XPS, N<sub>2</sub> sorption, DR UV-vis, PL spectroscopy and photoelectrochemical measurement.

Fig. 1(a) describes the XRD patterns of as-synthesized SmAn(300) composite photocatalysts. It could be found that the characteristic diffraction peaks perfectly indexed to the SrTiO<sub>3</sub> (JCPDS No. 35-0734) and Ag<sub>3</sub>PO<sub>4</sub> (JCPDS No. 06-0505) could be clearly observed in the XPD patterns of pure 3DOM-SrTiO<sub>3</sub> and Ag<sub>3</sub>PO<sub>4</sub>. With the increase of the molar ratio of 3DOM-SrTiO<sub>3</sub>, the intensities of diffraction peaks of SrTiO<sub>3</sub> increased gradually, while the intensities of Ag<sub>3</sub>PO<sub>4</sub> diffraction peaks decreased evidently. No additional diffraction peaks were observed in the XRD patterns of these SmAn(300) composites. The XRD patterns of S35A65(x) samples with different pore sizes and DS35A65 are shown in Fig. 1(b). The very similar patterns could be observed for these samples, which indicated the similar composition and crystallinity of these photocatalysts.

The SEM micrographs of obtained 3DOM-SrTiO<sub>3</sub>(x), Ag<sub>3</sub>PO<sub>4</sub>, and SmAn(x) composites are shown in Fig. 2. It could be observed from Fig. 2(a)–(c) that these 3DOM-SrTiO<sub>3</sub>(x) materials exhibited well-ordered inverse opal structures, and their average pore diameters were about 110 nm, 185 nm and 270 nm, respectively, which had a shrinkage of ~39% compared with the PMMA colloidal crystal

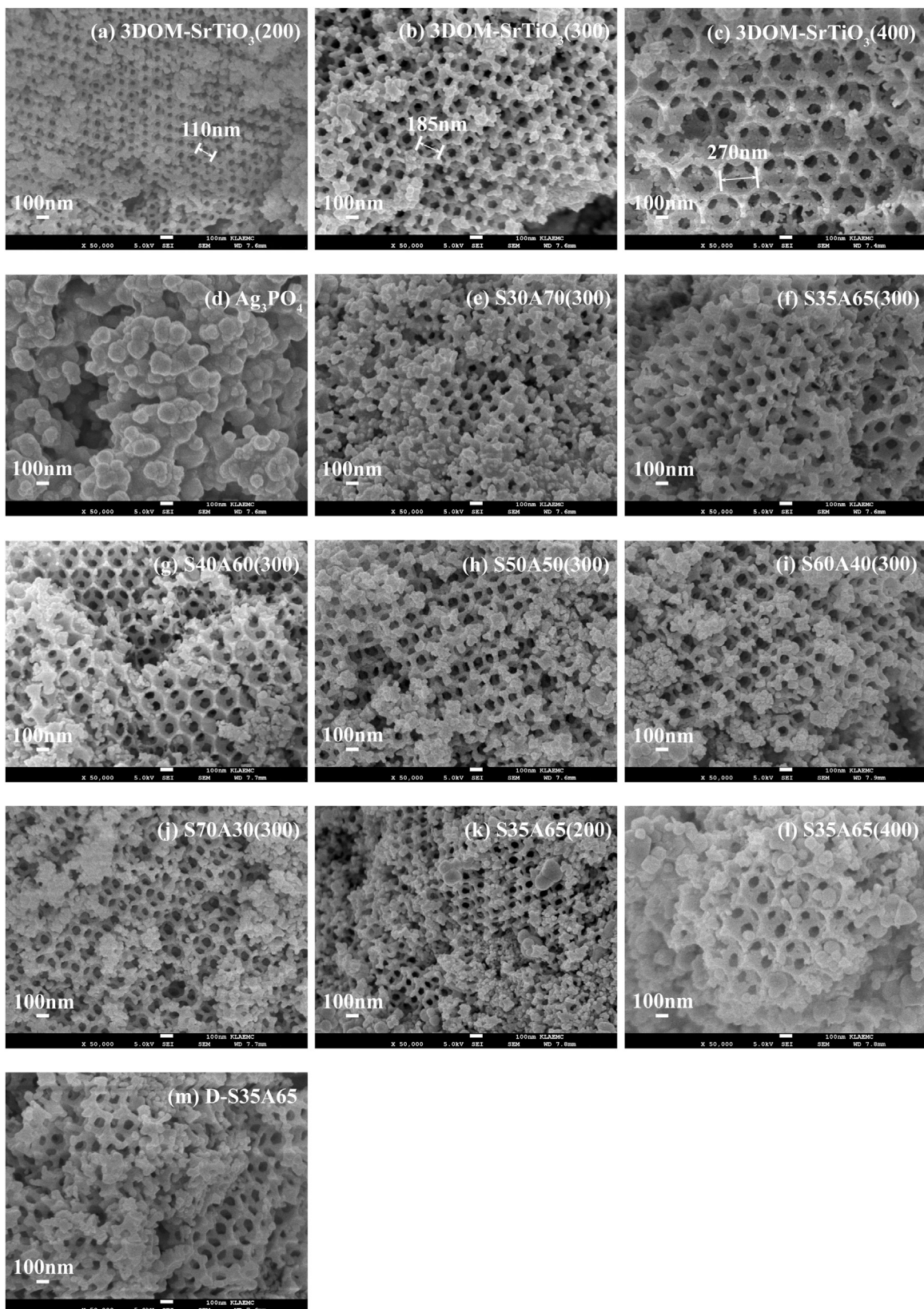


**Fig. 2.** SEM micrographs of (a–c) 3DOM-SrTiO<sub>3</sub>(x), (d) Ag<sub>3</sub>PO<sub>4</sub>, (e–l) SmAn(x), and (m) D-S35A65 photocatalysts.

templates. Fig. 2(d) exhibited the sphere-like sharp of nano Ag<sub>3</sub>PO<sub>4</sub> catalyst with a diameter of 80–200 nm. For the SmAn(300) composites, as shown in Fig. 2(e)–(i), with the increase of the molar ratio of Ag<sub>3</sub>PO<sub>4</sub>, more Ag<sub>3</sub>PO<sub>4</sub> particles with a diameter of 20–50 nm

were gathered into the macropores of 3DOM-SrTiO<sub>3</sub>(300). Moreover, the well-ordered three-dimensionally ordered macroporous structures of 3DOM-SrTiO<sub>3</sub>(300) were well maintained. Similarly with S35A65(300), S35A65(200) and S35A65(400) composites (as

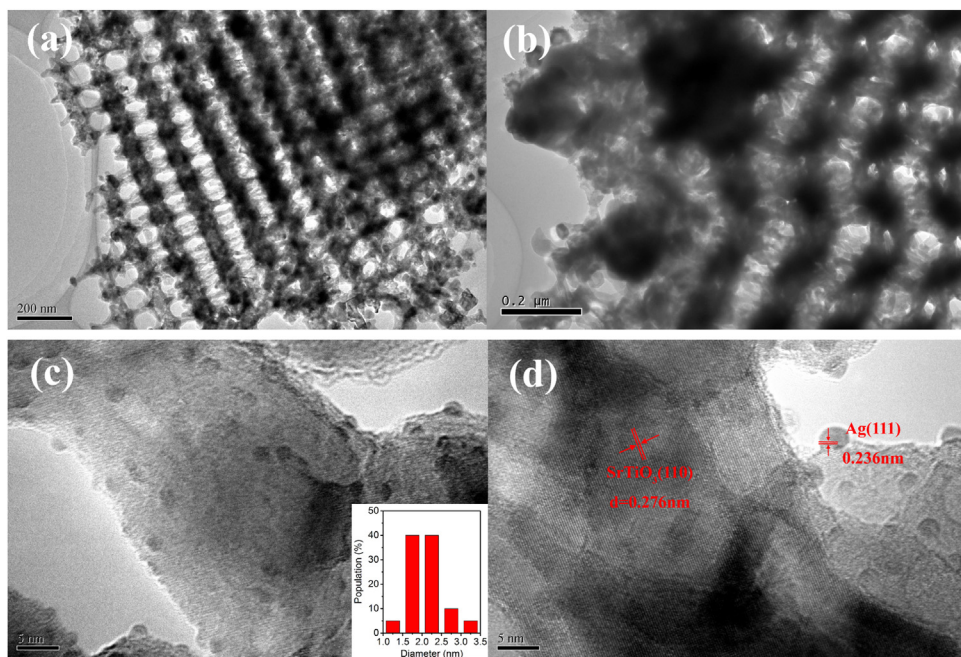


**Fig. 3.** TEM and HRTEM images of (a) 3DOM-SrTiO<sub>3</sub>(300) and (b-d) S35A65(300) composites.

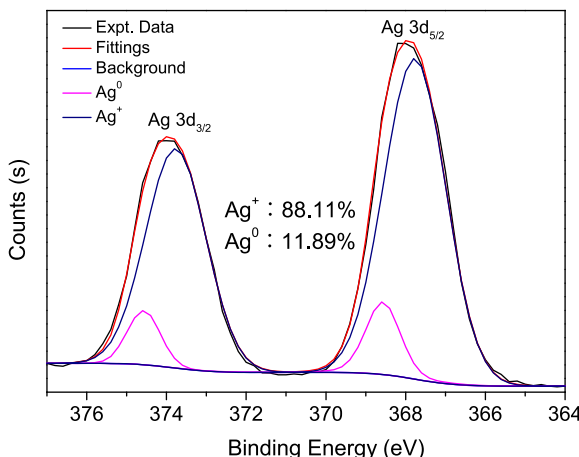


**Fig. 4.** XPS spectrum of Ag 3d over S35A65(300) composite.

shown in Fig. 2(j) and (k)) also exhibited well designed structure. Fig. 2(l) displays the morphology of DS35A65, the nano sized SrTiO<sub>3</sub> particles with an average diameter of 75 nm were homogeneous compositized with Ag<sub>3</sub>PO<sub>4</sub> nano particles.

The HRTEM images of S35A65(300) composites are shown in Fig. 3. It could be clearly observed that the Ag<sub>3</sub>PO<sub>4</sub> nano particles were mainly deposited into the macropores of 3DOM-SrTiO<sub>3</sub>. The interplanar distance of 3DOM-SrTiO<sub>3</sub> was 0.276 nm, which was corresponding to the lattice spacing of the (110) plane of SrTiO<sub>3</sub>. Some metallic Ag nanoparticles with an average diameter of ~2 nm were detected on the surface of Ag<sub>3</sub>PO<sub>4</sub>, which was generated through a photo corrosion reaction of Ag<sub>3</sub>PO<sub>4</sub> (Ag<sup>+</sup> + e<sup>-</sup> → Ag<sup>0</sup>) [51,59,75]. The HRTEM characterization results indicated the ternary composite structure of these obtained 3DOM-SrTiO<sub>3</sub>/Ag/Ag<sub>3</sub>PO<sub>4</sub> photocatalysts.

These S35A65(x) composites were further detected by XPS scan of the Ag 3d region and the results are depicted in Figs. 4 and S4 (Supplementary Materials). The Ag 3d<sub>5/2</sub> and Ag 3d<sub>3/2</sub> peaks near 368 and 374 eV could be observed, which could be fitted to four separated peaks corresponding to metallic Ag<sup>0</sup> and Ag<sup>+</sup>

**Table 2**  
The BET surface areas of these obtained composite photocatalysts.

Sample	S <sub>BET</sub> (m <sup>2</sup> g <sup>-1</sup> )
Ag <sub>3</sub> PO <sub>4</sub>	1.29
S30A70(300)	9.15
S35A65(300)	10.58
S40A60(300)	11.97
S50A50(300)	14.32
S60A40(300)	16.11
S70A30(300)	23.08
3DOM-SrTiO <sub>3</sub> (300)	28.96
S35A65(200)	11.34
S35A65(400)	9.96
DS35A65	9.72

ions [75,78–80]. The amount of metallic Ag<sup>0</sup> on the surface of these composites were determined as 11.82%, 11.89%, and 11.85% for S35A65(200), S35A65(300), and S35A65(400), respectively. The XPS characterization of S35A65(x) catalysts further confirmed their ternary composite structure.

These SmAn(x) composites were characterized by N<sub>2</sub> sorption and their BET surface areas are listed in Table 2. It could be found that the BET surface areas of these SmAn(x) composites were in the range of 9.15–23.08 m<sup>2</sup> g<sup>-1</sup>. For the SmAn(300) composites, with the increase of Ag<sub>3</sub>PO<sub>4</sub> amount, the BET surface areas of SmAn(300) composites decreased gradually. It can be attributed to the lower BET surface areas of Ag<sub>3</sub>PO<sub>4</sub> nanoparticles (1.29 m<sup>2</sup> g<sup>-1</sup>) compared with 3DOM-SrTiO<sub>3</sub>(300) material (28.96 m<sup>2</sup> g<sup>-1</sup>). While, for the S35A65(x) composites, S35A65(200) exhibited the highest BET surface areas due to the smaller pore diameter of 3DOM-SrTiO<sub>3</sub>(200).

Fig. 5 describes the DR UV-vis spectra of SmAn(300) composites. It could be found that the optical absorption edge of 3DOM-SrTiO<sub>3</sub>(300) locates at around 380 nm. When 3DOM-SrTiO<sub>3</sub>(300) combining with Ag<sub>3</sub>PO<sub>4</sub>, the absorption edges of these SmAn(300) composites red-shifted to 508 nm, which could be attributed to the light absorption of Ag<sub>3</sub>PO<sub>4</sub> nanoparticles in SmAn(300) composites. The notably broadened light response ranges of these SmAn(300) composites should lead to the enhanced visible light photocatalytic activity.

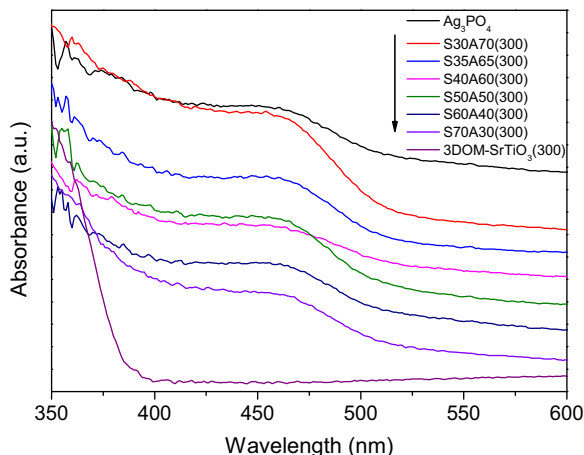


**Fig. 5.** DR UV-vis spectra of  $\text{Ag}_3\text{PO}_4$ , 3DOM-SrTiO<sub>3</sub>(300) and SmAn(300) composites.

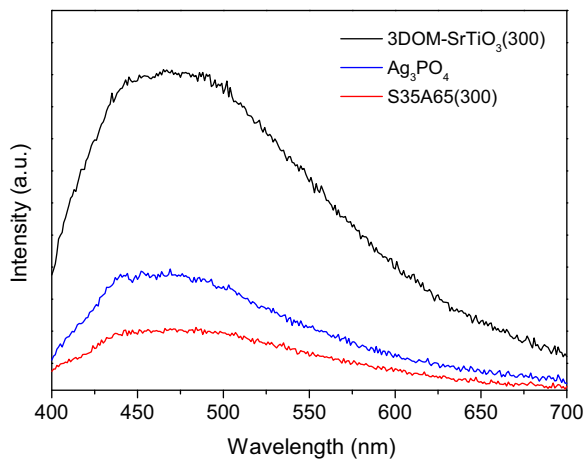


**Fig. 6.** PL spectra of 3DOM-SrTiO<sub>3</sub>(300),  $\text{Ag}_3\text{PO}_4$ , and S35A65(300).

The room temperature PL spectra of 3DOM-SrTiO<sub>3</sub>(300),  $\text{Ag}_3\text{PO}_4$  and S35A65(300) are shown in Fig. 6. The samples were excited at the wavelength of 374 nm and their photoluminescence emission spectra showed a broad band from 450 to 500 nm within visible light region. In comparison with the other two photocatalysts, S35A65(300) exhibited the lowest emission intensity, which indicated that the recombination of photogenerated electrons and holes was effectively prevented in the catalyst S35A65(300).

Fig. 7 describes the current-time ( $I-t$ ) curves of S35A65(300) and  $\text{Ag}_3\text{PO}_4$  photocatalysts under visible-light irradiation. Compared with pure  $\text{Ag}_3\text{PO}_4$ , S35A65(300) exhibited greater photocurrent generation efficiency obviously. The photocurrent density of the S35A65(300) photocatalyst was about 3 times larger than that of pure  $\text{Ag}_3\text{PO}_4$ . This should be ascribed to the larger light conversion efficiency and lower recombination rate of photogenerated carriers of S35A65(300). It was well consistent with the result of PL spectra.

### 3.2. Effect of molar ratio of 3DOM-SrTiO<sub>3</sub> to $\text{Ag}_3\text{PO}_4$ on the catalytic performance

The influence of SrTiO<sub>3</sub>: $\text{Ag}_3\text{PO}_4$  molar ratio on the catalytic performance of SmAn(300) composites was investigated in this section choosing RhB (10 ppm) as the model organic contaminant under visible light irradiation. The degradation curves are described in Fig. 8. For comparison, pure  $\text{Ag}_3\text{PO}_4$  and 3DOM-SrTiO<sub>3</sub>(300) were also employed as catalyst in these experiments. Before light irradiation, an adsorption process of RhB was carried out for 30 min to reach the adsorption-desorption equilibration.

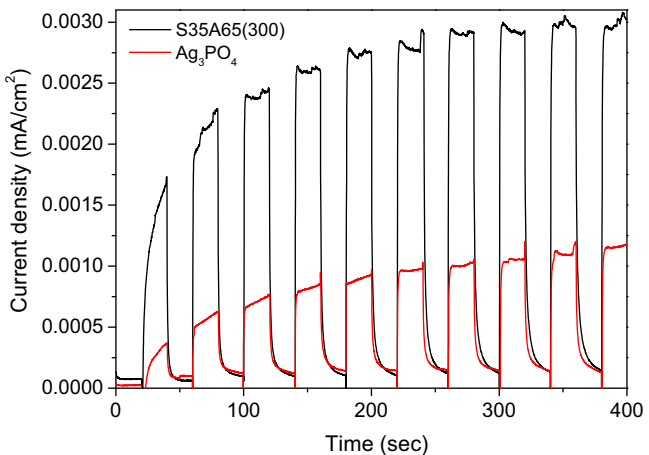


**Fig. 7.** Current-time ( $I-t$ ) curves of S35A65(300) and  $\text{Ag}_3\text{PO}_4$  photocatalysts.

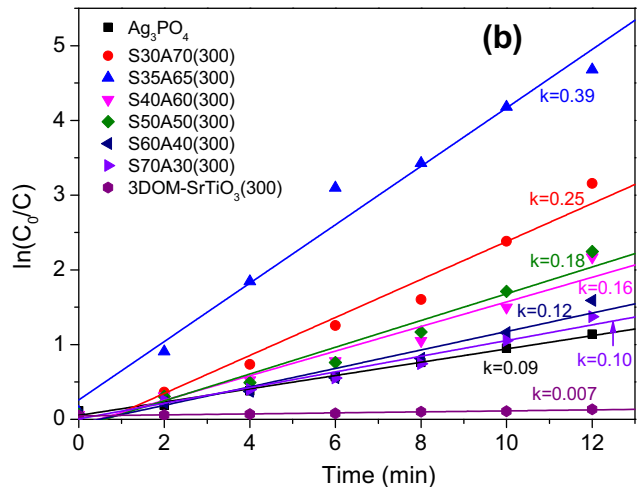
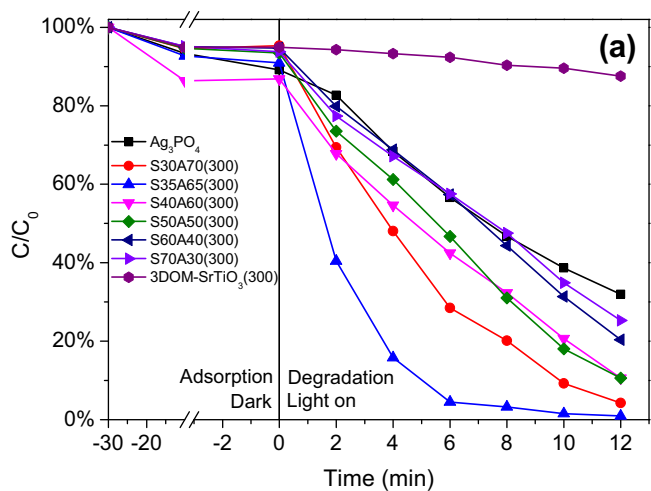


**Fig. 8.** Photocatalytic activities of  $\text{Ag}_3\text{PO}_4$ , SmAn(300) and 3DOM-SrTiO<sub>3</sub>(300) for visible light degradation of RhB(10 ppm).

As shown in Fig. 8(a), all the SmAn(300) photocatalysts exhibited higher photocatalytic activity than both  $\text{Ag}_3\text{PO}_4$  and 3DOM-SrTiO<sub>3</sub>(300). Among these SmAn(300) composite photocatalysts, S35A65(300) exhibited the most excellent photocatalytic performance for RhB degradation, which could completely decompose

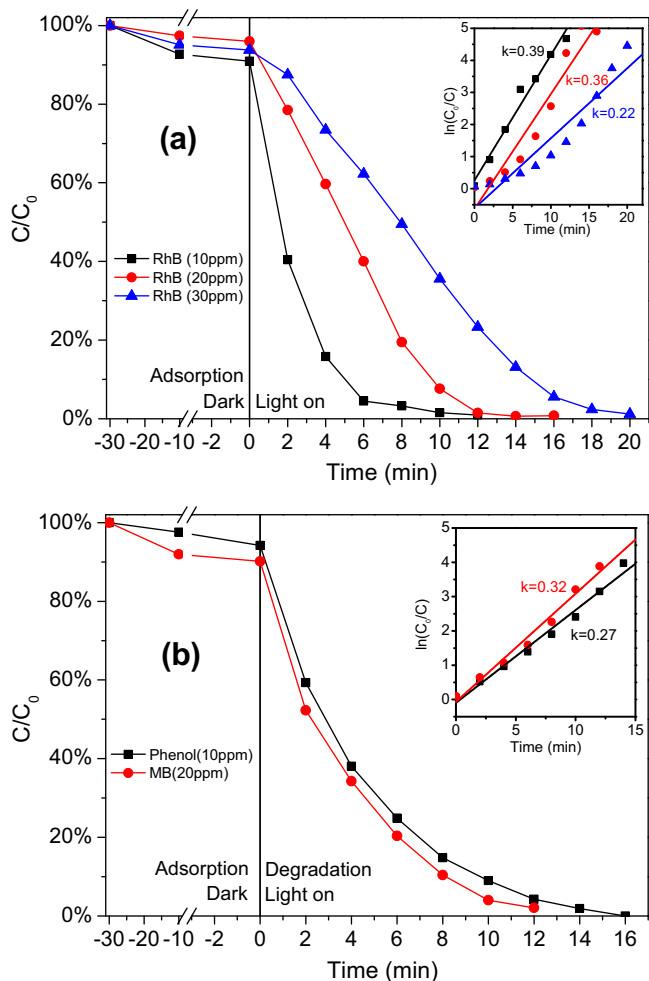


**Fig. 9.** Photocatalytic activities of S35A65( $x$ ) and D-S35A65 for visible light degradation of RhB(10 ppm).

RhB within 12 min. While, only 68.0% and 12.4% of RhB could be degraded at the same irradiation time over  $\text{Ag}_3\text{PO}_4$  and 3DOM-SrTiO<sub>3</sub>(300), respectively. The notably enhanced photocatalytic performance of S35A65(300) compared with single  $\text{Ag}_3\text{PO}_4$  and 3DOM-SrTiO<sub>3</sub>(300) could be mainly attributed to the efficient separation of photogenerated electron-hole pairs, which had been well demonstrated by PL spectra.

The photodegradation kinetic constants of different samples can be measured by the pseudo first-order equation [ $\ln(C_0/C) = kt$ ], where  $k$  is the apparent kinetic rate constants,  $t$  is the irradiation time,  $C$  and  $C_0$  are the real-time concentration at  $t$  and the initial concentration of the organic dyes, respectively. As illustrated in Fig. 8(b), the apparent rate constant of S35A65(300) was  $0.39 \text{ min}^{-1}$ , which was 4.3 times as high as that of  $\text{Ag}_3\text{PO}_4$  ( $0.09 \text{ min}^{-1}$ ) and 55.7 times higher than that of 3DOM-SrTiO<sub>3</sub>(300) ( $0.007 \text{ min}^{-1}$ ). 3DOM-SrTiO<sub>3</sub>(300) exhibited extremely low catalytic activity under visible light irradiation because of its wide band gap (ca. 3.24 eV estimated from the DR UV-vis spectra).

In order to gain better insight into the catalytic performance of the S35A65(300) composites, RhB (20 ppm, 30 ppm), phenol (10 ppm) and MB (20 ppm) were also employed as target contaminants. Fig. 9(a) depicts the degradation and kinetic data curves of RhB with different initial concentration over S35A65(300) under visible light irradiation. It could be found that with the increase of RhB initial concentration from 10 ppm to 30 ppm, the complete degradation time of RhB was prolonged from 12 min to 20 min. The degradation and kinetic data curves of phenol and MB

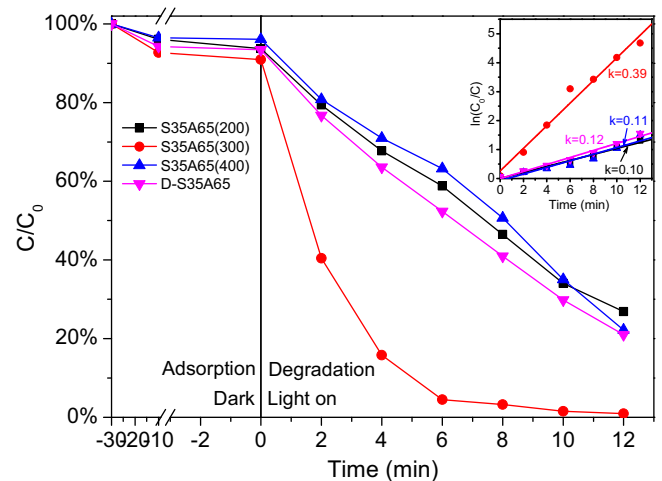


**Fig. 10.** Photodegradation of organic contaminants under visible light irradiation catalyzed by S35A65(300).

over S35A65(300) are shown in Fig. 9(b). Through 16 min visible light irradiation, 10 ppm of phenol could be completely decomposed, which further confirmed the excellent visible-light-driven photocatalytic performance of S35A65(300) for different organic contaminants.

### 3.3. Effect of stop-band of 3DOM-SrTiO<sub>3</sub> on the catalytic performance of 3DOM-SrTiO<sub>3</sub>/Ag/ $\text{Ag}_3\text{PO}_4$ composites

The influence of stop-bands of 3DOM-SrTiO<sub>3</sub> on the catalytic performance of 3DOM-SrTiO<sub>3</sub>/Ag/ $\text{Ag}_3\text{PO}_4$  composites was investigated in this section. Fig. 10 depicts the degradation and kinetic data curves of RhB (10 ppm) over S35A65(200), S35A65(300), S35A65(400) and D-S35A65 under visible-light irradiation. It could be found that S35A65(300) achieved the highest photocatalytic performance among these photocatalysts. Meanwhile, S35A65(200), S35A65(400) and D-S35A65 exhibited comparable catalytic performance for RhB degradation. The apparent rate constant of S35A65(300) was nearly 4 times higher than that of S35A65(200), S35A65(400), and D-S35A65. This indicated that a more significant enhancement effect was performed on S35A65(300) photocatalysts.

$$\lambda_{\max} = 2 \sqrt{\frac{2}{3}} D \sqrt{n_{\text{SrTiO}_3}^2 f + n_{\text{water}}^2 (1-f) \sin^2 \theta} \quad (1)$$

In order to provide insights into the mechanism of slow photon effect on photocatalytic performance of 3DOM-SrTiO<sub>3</sub>/Ag/ $\text{Ag}_3\text{PO}_4$  composites. The stop-bands of 3DOM-SrTiO<sub>3</sub> materials with different pore sizes were calculated through the modified Bragg's law (as described in Eq. (1)) [50,81,82]. In this equation,  $\lambda_{\max}$  represents the stop-band wavelength,  $D$  means the pore diameter of 3DOM-SrTiO<sub>3</sub>,  $n$  express the refractive index of different medium,  $f$  is the SrTiO<sub>3</sub> phase volume percentage (for an fcc structure, generally  $f=0.26$ ), and the meaning of  $\theta$  is the incident angle of light. Because the photocatalyst powder was directly suspended in reaction solution, the incident angle of light irradiation to the photocatalysts should be varied over a wide range from  $0^\circ$  to  $90^\circ$ . Thus the calculated stop-bands of 3DOM-SrTiO<sub>3</sub>(200) ( $D=110 \text{ nm}$ ), 3DOM-SrTiO<sub>3</sub>(300) ( $D=200 \text{ nm}$ ), and 3DOM-SrTiO<sub>3</sub>(400) ( $D=270 \text{ nm}$ ) were in the ranges of 243–302 nm, 440 ~ 548 nm, and 594–740 nm, respectively.

As described in Fig. 11, the calculated stop-bands of 3DOM-SrTiO<sub>3</sub> materials were depicted in the DR UV-vis spectra of S35A65(200), S35A65(300), and S35A65(400) using different color.

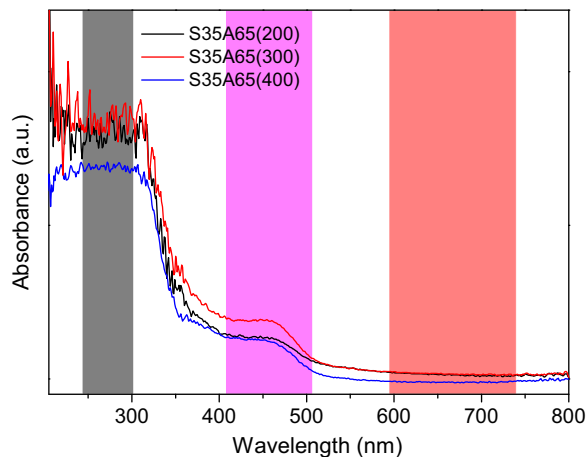


**Fig. 11.** DR UV-vis spectra of S35A65(x) photocatalysts and the calculated stop-bands of 3DOM-SrTiO<sub>3</sub>(200) (gray), 3DOM-SrTiO<sub>3</sub>(300) (purple), and 3DOM-SrTiO<sub>3</sub>(400) (red). (For interpretation of the references to colour in this figure legend, the reader is referred to the web version of this article.)

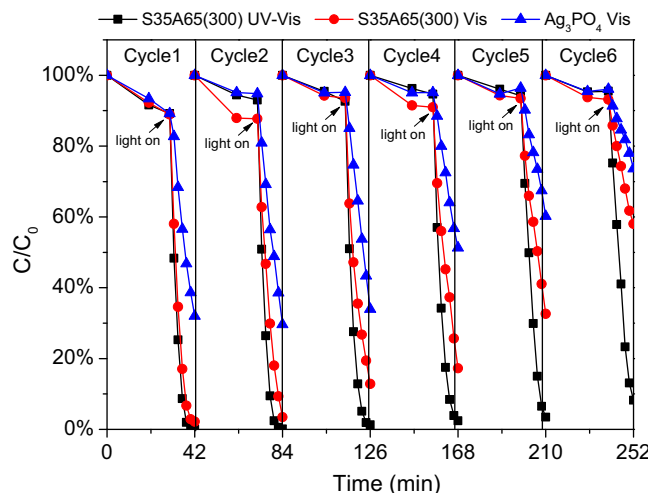


**Fig. 12.** Cycling tests of S35A65(300) for photodegradation of RhB(10 ppm) under visible light (300W) or UV-vis light (210W) irradiation.

The incident light with certain wavelength in the range of stop-band could be reflected into the macropores of 3DOM-SrTiO<sub>3</sub> materials. The slow photons were limited into the photocatalyst via multiple scattering and diffraction, which could lead to the enhancement of photon-matter interaction. The stop-band of 3DOM-SrTiO<sub>3</sub>(300) was determined in the range of 440~548 nm. Meanwhile, S35A65(300) photocatalyst exhibited an obvious optical absorption band in this range according to the DR UV-vis spectrum. This would result in the significant enhanced photocatalytic performance of S35A65(300) photocatalyst. However, the stop-bands of S35A65(200) and S35A65(400) were located in the region that could not be utilized for these photocatalysts in this visible-light photocatalysis experiment system. Therefore, compared with S35A65(200) and S35A65(400), S35A65(300) exhibited the highest photocatalytic activity.

#### 3.4. Photocatalytic stability of the 3DOM-SrTiO<sub>3</sub>/Ag/Ag<sub>3</sub>PO<sub>4</sub> composites

S35A65(300) was used as the model catalyst to evaluate the photocatalytic stability of the 3DOM-SrTiO<sub>3</sub>/Ag/Ag<sub>3</sub>PO<sub>4</sub> composites. As depicted in Fig. 12, under visible-light irradiation, the S35A65(300) exhibited gradually decreased catalytic performance

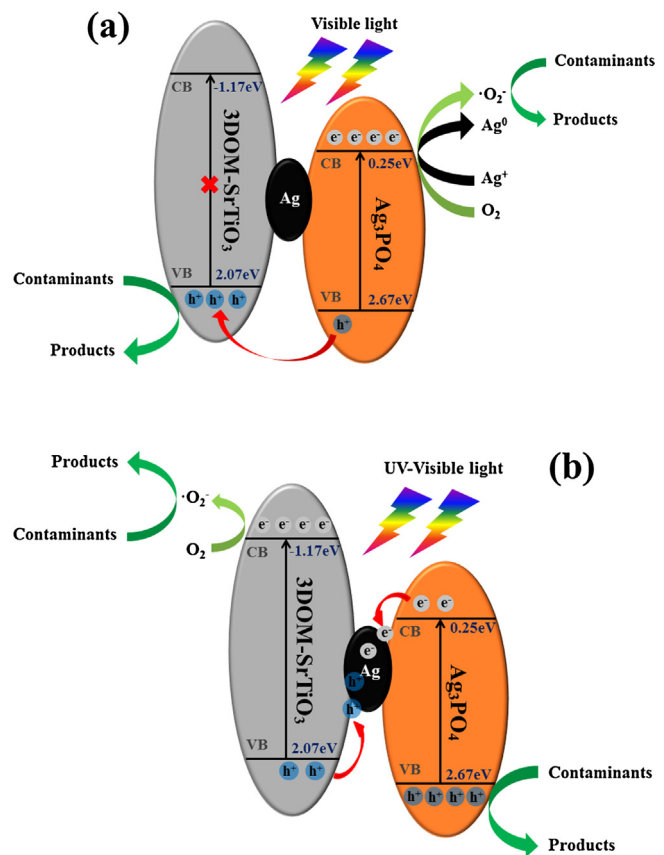


**Fig. 13.** Schematic diagrams of band structures and proposed mechanisms of the 3DOM-SrTiO<sub>3</sub>/Ag/Ag<sub>3</sub>PO<sub>4</sub> composites under (a) visible light irradiation and (b) UV-vis light irradiation.

for RhB (10 ppm) degradation, which was very similar with the Ag<sub>3</sub>PO<sub>4</sub> photocatalyst. At the sixth cycle, the degradation efficiency of RhB reduced to 42.0% for 12 min. The decreased photocatalytic performance of S35A65(300) under visible light irradiation could be mainly attributed to the photocorrosion of Ag<sub>3</sub>PO<sub>4</sub>.

However, it is interesting that S35A65(300) exhibited excellent reusability under UV-vis light irradiation. It must be emphasized that the luminous power was reduced to 210 W for UV-vis light source to keep the photocatalytic activity consistent at the first cycle under different light source irradiation. It could be found from Fig. 12, no obvious decrease of the efficiency of S35A65(300) was observed under UV-vis light irradiation for six times. The degradation efficiency of RhB still reached 91.8% at the sixth cycle.

#### 3.5. Enhancement mechanism of photocatalytic activity and stability of 3DOM-SrTiO<sub>3</sub>/Ag/Ag<sub>3</sub>PO<sub>4</sub> composites

In order to provide an insight into the notably enhanced photocatalytic activity and stability of 3DOM-SrTiO<sub>3</sub>/Ag/Ag<sub>3</sub>PO<sub>4</sub> composites, the schematic diagrams of band structure of S35A65(300) are depicted in Fig. 13 and the possible reaction mechanism is proposed. The conduction band (CB) and valence band (VB) edges of these semiconductors, designated as E<sub>CB</sub> and E<sub>VB</sub>, were calculated by the following equations [83–86].

$$E_{VB} = \chi - E_0 + 1/2E_g \quad (2)$$

$$E_{CB} = \chi - E_0 - 1/2E_g \quad (3)$$

In these equations,  $\chi$  is the absolute electronegativity of the semiconductor,  $E_0$  is the energy of free electrons on the hydrogen scale (generally  $E_0 = 4.5$  eV), and  $E_g$  is the bandgap energy of

these semiconductors. In present work,  $E_g$  of  $\text{Ag}_3\text{PO}_4$  and 3DOM-SrTiO<sub>3</sub>(300) were estimated from the  $(\alpha h\nu)^2 \sim h\nu$  plot of DR UV-vis characterization, which were 2.42 eV and 3.24 eV, respectively. Thus, the calculated  $E_{\text{CB}}$  and  $E_{\text{VB}}$  of 3DOM-SrTiO<sub>3</sub>(300) were -1.17 and 2.07 eV, respectively. And those of  $\text{Ag}_3\text{PO}_4$  were calculated to be 0.25 and 2.67 eV, separately.

As shown in Fig. 13(a), when S35A65(300) was irradiated by visible light,  $\text{Ag}_3\text{PO}_4$  could be excited but 3DOM-SrTiO<sub>3</sub>(300) could not. Because the  $E_{\text{VB}}$  of  $\text{Ag}_3\text{PO}_4$  was more positive than that of 3DOM-SrTiO<sub>3</sub>(300), the photogenerated holes on  $\text{Ag}_3\text{PO}_4$  could be transferred from  $\text{Ag}_3\text{PO}_4$  to 3DOM-SrTiO<sub>3</sub>(300), which could directly oxidize the organic contaminants. While, the photogenerated electrons would be remained on the CB of  $\text{Ag}_3\text{PO}_4$ . The improved separation efficiency of photogenerated carriers led to the enhanced photocatalytic performance of S35A65(300) compared with single  $\text{Ag}_3\text{PO}_4$  and 3DOM-SrTiO<sub>3</sub>(300). However, the accumulated electrons on CB of  $\text{Ag}_3\text{PO}_4$  would be consumed through a reduction reaction of  $\text{Ag}^+$  to produce metallic  $\text{Ag}^0$ , which led to the decreased activity of S35A65(300) under visible-light-driven cycling experiments.

Meanwhile, when S35A65(300) was irradiated by UV-vis light (as shown in Fig. 13(b)), both  $\text{Ag}_3\text{PO}_4$  and 3DOM-SrTiO<sub>3</sub>(300) could be excited to produce photogenerated charge carriers. Because the  $E_{\text{CB}}$  of  $\text{Ag}_3\text{PO}_4$  was more negative than the Fermi level of Ag [87], and the  $E_{\text{VB}}$  of 3DOM-SrTiO<sub>3</sub>(300) was more positive than the Fermi level of Ag [88], the photogenerated electrons in CB of  $\text{Ag}_3\text{PO}_4$  and the photogenerated holes in VB of 3DOM-SrTiO<sub>3</sub>(300) could migrate to Ag nanoparticles simultaneously and combined with each other, which resulted in a typical Z-scheme mechanism. As a result, the photogenerated electrons in the CB of  $\text{Ag}_3\text{PO}_4$  were consumed and the photocorrosion of  $\text{Ag}_3\text{PO}_4$  was suppressed. That's the reason that the stability of S35A65(300) was notably improved under UV-vis light irradiation. The photogenerated holes in the VB of  $\text{Ag}_3\text{PO}_4$  could directly oxidize the contaminants. Moreover, the photogenerated electrons in the CB of 3DOM-SrTiO<sub>3</sub>(300) could be captured by adsorbed oxygen to form  $\bullet\text{O}_2^-$ , which was also considered as an effective active species in photocatalytic degradation of organic contaminants.

In order to further confirm the active oxygen species of 3DOM-SrTiO<sub>3</sub>/Ag/ $\text{Ag}_3\text{PO}_4$  ternary composites under visible and UV-vis light irradiation, the ESR spin-trap signals of S35A65(300) with DMPO in methanol solution (for DMPO-•O<sub>2</sub><sup>-</sup>) or aqueous solution (for DMPO-•OH) were detected according to the reported methods[89,90], and the results are shown in Fig. 14. It could be found that negligible signals of DMPO-•OH (Fig. 14(b)) but obvious DMPO-•O<sub>2</sub><sup>-</sup> signals (Fig. 14(a)) were detected over S35A65(300) under visible light or UV-vis light irradiation. Although  $\text{h}^+$  was considered as the mainly active species for  $\text{Ag}_3\text{PO}_4$ , •O<sub>2</sub><sup>-</sup> could also be detected over  $\text{Ag}_3\text{PO}_4$  catalyzed photodegradation reactions [91–93], which was agreed with the controlling photodegradation experiments in the presence of different scavenger (as shown in Fig. S5 of the Supplementary Materials). Moreover, the slightly higher signal intensity of DMPO-•O<sub>2</sub><sup>-</sup> under UV-vis light irradiation were detected compared with that obtained under visible light irradiation, which suggesting the generation of more •O<sub>2</sub><sup>-</sup> in Z-scheme process under UV-vis light irradiation. The ESR characterization and controlling experiment results further confirmed the active species of 3DOM-SrTiO<sub>3</sub>/Ag/ $\text{Ag}_3\text{PO}_4$  composites which has been described in Fig. 13.

In addition, the Ag 3d XPS characterization of used S35A65(300) photocatalysts through six cycling experiments under visible light or UV-vis light irradiation was performed to investigate the reason of photocatalyst deactivation. It could be found from Fig. 15, the Ag 3d<sub>5/2</sub> and Ag 3d<sub>3/2</sub> peaks near 368 and 374 eV could be fitted to two separate peaks corresponding to  $\text{Ag}^0$  and  $\text{Ag}^+$  ions. When the S35A65(300) photocatalysts was irradiated by visible

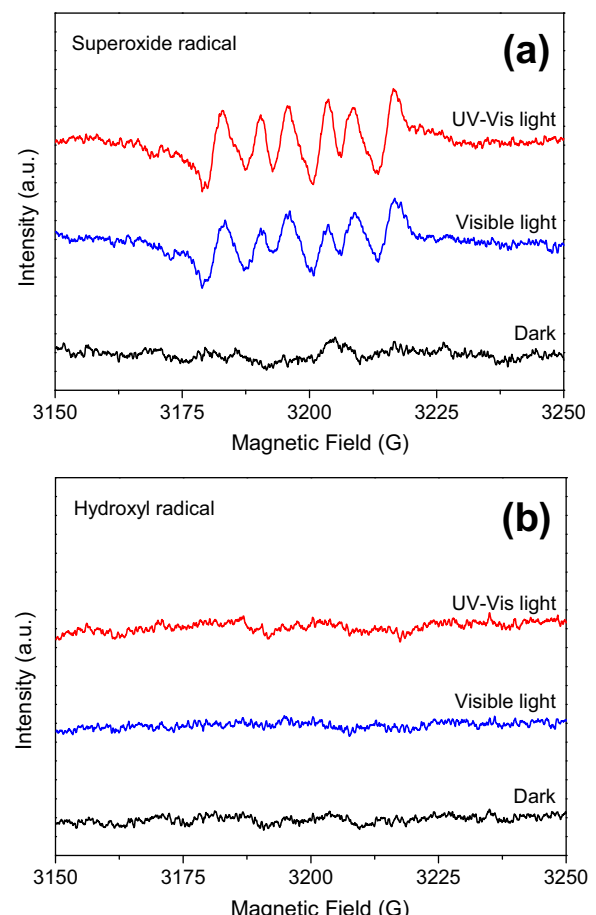


**Fig. 14.** ESR spin-trap signals of S35A65(300) with DMPO in (a) methanol solution (for DMPO-•O<sub>2</sub><sup>-</sup>) and (b) aqueous solution (for DMPO-•OH) under visible light or UV-vis light irradiation.

light, about 40% of metallic Ag was formed on the surface of catalyst through six cycling experiments. However, when UV-vis light was used as light source in the photocatalytic reaction, only 24% of metallic Ag was detected on the surface of S35A65(300) after six cycling experiments, which meant the photocorrosion of  $\text{Ag}_3\text{PO}_4$  was suppressed. The XPS characterization results of used S35A65(300) photocatalysts further confirmed the Z-scheme mechanism of 3DOM-SrTiO<sub>3</sub>/Ag/ $\text{Ag}_3\text{PO}_4$  composites under UV-vis light irradiation.

#### 4. Conclusions

In summary, the 3DOM-SrTiO<sub>3</sub>/Ag/ $\text{Ag}_3\text{PO}_4$  ternary composite photocatalysts were originally synthesized and well characterized by XRD, SEM, TEM, DR UV-vis, XPS, PL spectroscopy, N<sub>2</sub> sorption, and photoelectrochemical measurement. Compared with single 3DOM-SrTiO<sub>3</sub> and  $\text{Ag}_3\text{PO}_4$ , the obtained 3DOM-SrTiO<sub>3</sub>/Ag/ $\text{Ag}_3\text{PO}_4$  ternary composites exhibited notably enhanced photocatalytic performance for visible light degradation of RhB, phenol, and MB, which could be attributed to the increased separate efficiency of photogenerated electron-hole pairs. Moreover, the effect of stop-bands of 3DOM-SrTiO<sub>3</sub> materials was studied. Among these S35A65(x) catalysts, S35A65(300) exhibited the highest photocatalytic activity due to the suitable stop-bands of 3DOM-SrTiO<sub>3</sub>(300) material, which could significantly improve the photon-matter interaction. In addition, S35A65(300) exhibited excellent stability for RhB degradation under UV-vis light irradiation, although relatively lower stability of S35A65(300) was obtained under visible

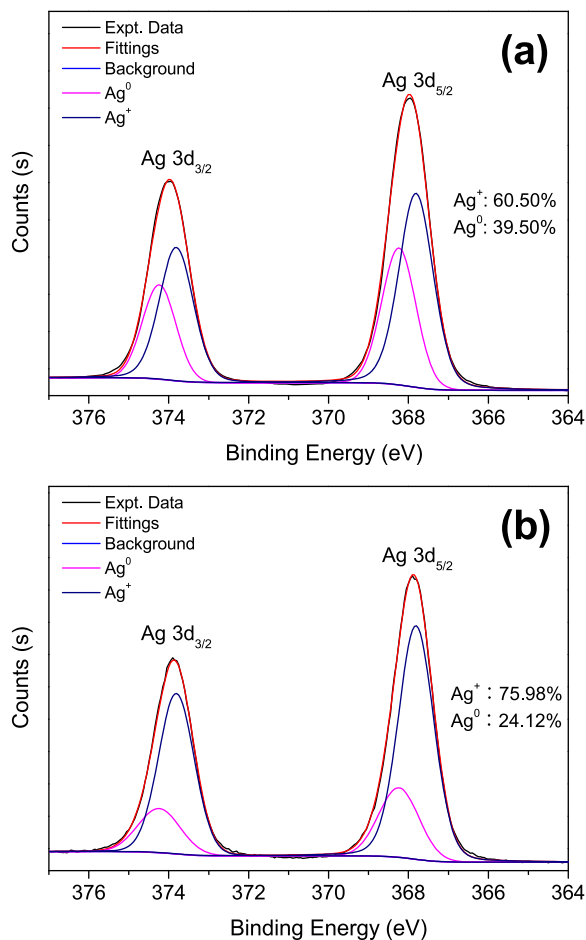


**Fig. 15.** High-resolution Ag 3d XPS spectra of used S35A65(300) photocatalyst after six cycles (a) under visible light and (b) under UV-vis light irradiation.

light irradiation. It could be explained by the Z-scheme mechanism of 3DOM-SrTiO<sub>3</sub>/Ag/Ag<sub>3</sub>PO<sub>4</sub> composites under UV-vis light irradiation, which could obviously decrease the photocorrosion of Ag<sub>3</sub>PO<sub>4</sub>.

## Acknowledgements

This work was supported by the National High Technology Research and Development Program of China (Grant No. 2012AA063008), the Tianjin Municipal Natural Science Foundation (Grant Nos. 14JCQNJC06000, 14JCZDJC32000 and 15JCTPJC63500), China Scholarship Council (Grant 201606200096), and the Fundamental Research Funds for the Central Universities.

## Appendix A. Supplementary data

Supplementary data associated with this article can be found, in the online version, at <http://dx.doi.org/10.1016/j.apcatb.2017.03.058>.

## References

- [1] N.S. Lewis, Nature 414 (2001) 589–590.
- [2] R. Schloegl, Nat. Mater. 7 (2008) 772–774.
- [3] A. Kudo, Y. Miseki, Chem. Soc. Rev. 38 (2009) 253–278.
- [4] H. Tong, S. Ouyang, Y. Bi, N. Umezawa, M. Oshikiri, J. Ye, Adv. Mater. 24 (2012) 229–251.
- [5] J. Di, J. Xia, Y. Ge, H. Li, H. Ji, H. Xu, Q. Zhang, H. Li, M. Li, Appl. Catal. B: Environ. 168–169 (2015) 51–61.
- [6] J. Di, J. Xia, S. Yin, H. Xu, L. Xu, Y. Xu, M. He, H. Li, J. Mater. Chem. A 2 (2014) 5340–5351.
- [7] E. Grabowska, Appl. Catal. B: Environ. 186 (2016) 97–126.
- [8] Y. Sakata, Y. Miyoshi, T. Maeda, K. Ishikiriyama, Y. Yamazaki, H. Imamura, Y. Ham, T. Hisatomi, J. Kubota, A. Yamakata, K. Domen, Appl. Catal. A: Gen. 521 (2016) 227–232.
- [9] U. Sulaiman, S. Yin, T. Sato, Appl. Catal. B: Environ. 105 (2011) 206–210.
- [10] R. Niishiro, S. Tanaka, A. Kudo, Appl. Catal. B: Environ. 150–151 (2014) 187–196.
- [11] B. Wang, S. Shen, L. Guo, Appl. Catal. B: Environ. 166–167 (2015) 320–326.
- [12] G. Zhang, G. Liu, L. Wang, J.T.S. Irvine, Chem. Soc. Rev. 45 (2016) 5951–5984.
- [13] W. Wang, M.O. Tade, Z. Shao, Chem. Soc. Rev. 44 (2015) 5371–5408.
- [14] R. Konta, T. Ishii, H. Kato, A. Kudo, J. Phys. Chem. B 108 (2004) 8992–8995.
- [15] F. Li, K. Yu, L.-L. Lou, Z. Su, S. Liu, Mater. Sci. Eng. B 172 (2010) 136–141.
- [16] A. Jia, X. Liang, Z. Su, T. Zhu, S. Liu, J. Hazard. Mater. 178 (2010) 233–242.
- [17] H. Liu, X. Chen, S. Yan, Z. Li, Z. Zou, Eur. J. Inorg. Chem. 2014 (2014) 3731–3735.
- [18] Q. Kuang, S. Yang, ACS Appl. Mater. Interfaces 5 (2013) 3683–3690.
- [19] Y. Zhong, K. Ueno, Y. Mori, X. Shi, T. Oshikiri, K. Murakoshi, H. Inoue, H. Misawa, Angew. Chem. Int. Ed. 53 (2014) 10350–10354.
- [20] T.K. Townsend, N.D. Browning, F.E. Osterloh, ACS Nano 6 (2012) 7420–7426.
- [21] S. Ouyang, P. Li, H. Xu, H. Tong, L. Liu, J. Ye, ACS Appl. Mater. Interfaces 6 (2014) 22726–22732.
- [22] W. Wang, J. Chen, C. Li, W. Tian, Nat. Commun. 5 (2014) 4647–4654.
- [23] S. Yu, Y.H. Kim, S.Y. Lee, H.D. Song, J. Yi, Angew. Chem. Int. Ed. 53 (2014) 11203–11207.
- [24] C. Chen, Q. Dai, C. Miao, L. Xu, H. Song, RSC Adv. 5 (2015) 4844–4852.
- [25] S. Ouyang, H. Tong, N. Umezawa, J. Cao, P. Li, Y. Bi, Y. Zhang, J. Ye, J. Am. Chem. Soc. 134 (2012) 1974–1977.
- [26] H. Tan, Z. Zhao, W.-b. Zhu, E.N. Coker, B. Li, M. Zheng, W. Yu, H. Fan, Z. Sun, ACS Appl. Mater. Interfaces 6 (2014) 19184–19190.
- [27] M. Srinivasarao, D. Collings, A. Philips, S. Patel, Science 292 (2001) 79–83.
- [28] A. Stein, B.E. Wilson, S.G. Rudisill, Chem. Soc. Rev. 42 (2013) 2763–2803.
- [29] Y. Wei, J. Jiao, Z. Zhao, J. Liu, J. Li, G. Jiang, Y. Wang, A. Duan, Appl. Catal. B: Environ. 179 (2015) 422–432.
- [30] M. Curti, J. Schneider, D.W. Bahnemann, C.B. Mendive, J. Phys. Chem. Lett. 6 (2015) 3903–3910.
- [31] S. Nishimura, N. Abrams, B.A. Lewis, L.I. Halaoui, T.E. Mallouk, K.D. Benkstein, J. van de Lagemaat, A.J. Frank, J. Am. Chem. Soc. 125 (2003) 6306–6310.
- [32] S.-H.A. Lee, N.M. Abrams, P.G. Hoertz, G.D. Barber, L.I. Halaoui, T.E. Mallouk, J. Phys. Chem. B 112 (2008) 14415–14421.
- [33] Y. Li, F. Piret, T. Léonard, B.-L. Su, J. Colloid Interface Sci. 348 (2010) 43–48.
- [34] M. Wu, Y. Li, Z. Deng, B.-L. Su, ChemSusChem 4 (2011) 1481–1488.
- [35] M. Wu, A. Zheng, F. Deng, B.-L. Su, Appl. Catal. B: Environ. 138–139 (2013) 219–228.
- [36] D. Qi, L. Lu, Z. Xi, L. Wang, J. Zhang, Appl. Catal. B: Environ. 160–161 (2014) 621–628.
- [37] J.I.L. Chen, G. von Freymann, S.Y. Choi, V. Kitaev, G.A. Ozin, Adv. Mater. 18 (2006) 1915–1919.
- [38] M. Srinivasan, T. White, Environ. Sci. Technol. 41 (2007) 4405–4409.
- [39] Q. Li, J.K. Shang, J. Am. Ceram. Soc. 91 (2008) 660–663.
- [40] J.I.L. Chen, G.A. Ozin, J. Mater. Chem. 19 (2009) 2675–2678.
- [41] J. Xu, B. Yang, M. Wu, Z. Fu, Y. Lv, Y. Zhao, J. Phys. Chem. C 114 (2010) 15251–15259.
- [42] F. Sordello, C. Duca, V. Maurino, C. Minero, Chem. Commun. 47 (2011) 6147–6149.
- [43] Y. Lu, H. Yu, S. Chen, X. Quan, H. Zhao, Environ. Sci. Technol. 46 (2012) 1724–1730.
- [44] H. Zhao, M. Wu, J. Liu, Z. Deng, Y. Li, B.-L. Su, Appl. Catal. B: Environ. 184 (2016) 182–190.
- [45] F. Sordello, C. Minero, Appl. Catal. B: Environ. 163 (2015) 452–458.
- [46] Y. Wang, H. Dai, J. Deng, Y. Liu, H. Arandiyan, X. Li, B. Gao, S. Xie, Solid State Sci. 24 (2013) 62–70.
- [47] Y. Wang, H. Dai, J. Deng, Y. Liu, Z. Zhao, X. Li, H. Arandiyan, Chem. Eng. J. 226 (2013) 87–94.
- [48] K. Ji, J. Deng, H. Zang, J. Han, H. Arandiyan, H. Dai, Appl. Catal. B: Environ. 165 (2015) 285–295.
- [49] M. Sadakane, K. Sasaki, H. Kunioku, B. Ohtani, R. Abe, W. Ueda, J. Mater. Chem. 20 (2010) 1811–1818.
- [50] X. Chen, J. Ye, S. Ouyang, T. Kako, Z. Li, Z. Zou, ACS Nano 5 (2011) 4310–4318.
- [51] Y. Chang, K. Yu, C. Zhang, R. Li, P. Zhao, L.-L. Lou, S. Liu, Appl. Catal. B: Environ. 176 (2015) 363–373.
- [52] K. Ji, H. Dai, J. Deng, H. Zang, H. Arandiyan, S. Xie, H. Yang, Appl. Catal. B: Environ. 168–169 (2015) 274–282.
- [53] S.M. Kozlov, K.M. Neyman, J. Catal. 344 (2016) 507–514.
- [54] S. Sun, W. Wang, L. Zhang, J. Mater. Chem. 22 (2012) 19244–19249.
- [55] S.-L. Chen, A.-J. Wang, C. Dai, J.B. Benziger, X.-C. Liu, Chem. Eng. J. 249 (2014) 48–53.
- [56] L. Chen, L. Xie, M. Wang, X. Ge, J. Mater. Chem. A 3 (2015) 2991–2998.
- [57] X. Li, X. Zhang, X. Zheng, Y. Shao, M. He, P. Wang, X. Fu, D. Li, J. Mater. Chem. A 2 (2014) 15796–15802.
- [58] K. Yu, C. Zhang, Y. Chang, Y. Feng, Z. Yang, T. Yang, L.-L. Lou, S. Liu, Appl. Catal. B: Environ. 200 (2017) 514–520.
- [59] Z. Yi, J. Ye, N. Kikugawa, T. Kako, S. Ouyang, H. Stuart-Williams, H. Yang, J. Cao, W. Luo, Z. Li, Y. Liu, R.L. Withers, Nat. Mater. 9 (2010) 559–564.
- [60] Y. Bi, S. Ouyang, N. Umezawa, J. Cao, J. Ye, J. Am. Chem. Soc. 133 (2011) 6490–6492.

[61] Y. Bi, H. Hu, S. Ouyang, Z. Jiao, G. Lu, J. Ye, *Chem.—Eur. J.* 18 (2012) 14272–14275.

[62] Y. Bi, H. Hu, S. Ouyang, G. Lu, J. Cao, J. Ye, *Chem. Commun.* 48 (2012) 3748–3750.

[63] H. Hu, Z. Jiao, H. Yu, G. Lu, J. Ye, Y. Bi, *J. Mater. Chem. A* 1 (2013) 2387–2390.

[64] Z. Jiao, Y. Zhang, H. Yu, G. Lu, J. Ye, Y. Bi, *Chem. Commun.* 49 (2013) 636–638.

[65] D.J. Martin, N. Umezawa, X. Chen, J. Ye, J. Tang, *Energy Environ. Sci.* 6 (2013) 3380–3386.

[66] D.J. Martin, G. Liu, S.J.A. Moniz, Y. Bi, A.M. Beale, J. Ye, J. Tang, *Chem. Soc. Rev.* 44 (2015) 7808–7828.

[67] Y. Bi, S. Ouyang, J. Cao, J. Ye, *Phys. Chem. Chem. Phys.* 13 (2011) 10071.

[68] Y. Zhang, Z.-R. Tang, X. Fu, Y.-J. Xu, *Appl. Catal. B: Environ.* 106 (2011) 445–452.

[69] P. Dong, Y. Wang, B. Cao, S. Xin, L. Guo, J. Zhang, F. Li, *Appl. Catal. B: Environ.* 132–133 (2013) 45–53.

[70] S. Kumar, T. Surendar, A. Baruah, V. Shanker, *J. Mater. Chem. A* 1 (2013) 5333–5340.

[71] W. Teng, X. Li, Q. Zhao, G. Chen, *J. Mater. Chem. A* 1 (2013) 9060–9068.

[72] C. Cui, Y. Wang, D. Liang, W. Cui, H. Hu, B. Lu, S. Xu, X. Li, C. Wang, Y. Yang, *Appl. Catal. B: Environ.* 158–159 (2014) 150–160.

[73] X. Ma, H. Li, Y. Wang, H. Li, B. Liu, S. Yin, T. Sato, *Appl. Catal. B: Environ.* 158–159 (2014) 314–320.

[74] Z.-M. Yang, G.-F. Huang, W.-Q. Huang, J.-M. Wei, X.-G. Yan, Y.-Y. Liu, C. Jiao, Z. Wan, A. Pan, *J. Mater. Chem. A* 2 (2014) 1750–1756.

[75] J. Zhang, K. Yu, Y. Yu, L.-L. Lou, Z. Yang, J. Yang, S. Liu, *J. Mol. Catal. A: Chem.* 391 (2014) 12–18.

[76] J. Guo, S. Ouyang, P. Li, Y. Zhang, T. Kako, J. Ye, *Appl. Catal. B: Environ.* 134–135 (2013) 286–292.

[77] X. Guan, L. Guo, *ACS Catal.* 4 (2014) 3020–3026.

[78] H. Lin, H. Ye, B. Xu, J. Cao, S. Chen, *Catal. Commun.* 37 (2013) 55–59.

[79] Y. Liu, L. Fang, H. Lu, Y. Li, C. Hu, H. Yu, *Appl. Catal. B: Environ.* 115–116 (2012) 245–252.

[80] J. Cao, B. Luo, H. Lin, B. Xu, S. Chen, *J. Hazard. Mater.* 217–218 (2012) 107–115.

[81] M. Ren, R. Ravikrishna, K.T. Valsaraj, *Environ. Sci. Technol.* 40 (2006) 7029–7033.

[82] K. Zhang, Y. Liu, J. Deng, S. Xie, H. Lin, X. Zhao, J. Yang, Z. Han, H. Dai, *Appl. Catal. B: Environ.* 202 (2017) 569–579.

[83] J.-D. Huang, J.-Y. Liu, K.-L. Han, In: *J. Hydrogen Energy* 37 (2012) 17870–17881.

[84] H. Xu, Y. Xu, H. Li, J. Xia, J. Xiong, S. Yin, C. Huang, H. Wan, *Dalton Trans.* 41 (2012) 3387–3394.

[85] C. Li, P. Zhang, R. Lv, J. Lu, T. Wang, S. Wang, H. Wang, J. Gong, *Small* 9 (2013) 3951–3956.

[86] X. Guan, L. Guo, *ACS Catal.* 4 (2014) 3020–3026.

[87] Z. Chen, W. Wang, Z. Zhang, X. Fang, *J. Phys. Chem. C* 117 (2013) 19346–19352.

[88] Z. Zhang, J.T. Yates, *Chem. Rev.* 112 (2012) 5520–5551.

[89] J. Di, J. Xia, M. Ji, L. Xu, S. Yin, Z. Chen, H. Li, *J. Mater. Chem. A* 4 (2016) 5051–5061.

[90] J. Xia, J. Di, H. Li, H. Xu, H. Li, S. Guo, *Appl. Catal. B: Environ.* 181 (2016) 260–269.

[91] X. Yang, H. Cui, Y. Li, J. Qin, R. Zhang, H. Tang, *ACS Catal.* 3 (2013) 363–369.

[92] X.-Q. Liu, W.-J. Chen, H. Jiang, *Chem. Eng. J.* 308 (2017) 889–896.

[93] M. Ge, *Chin. J. Catal.* 35 (2014) 1410–1417.